In vivo fluorescence imaging with high-resolution microlenses

Robert P J Barretto[1], Bernhard Messerschmidt[2] & Mark J Schnitzer[1,3]

Micro-optics are increasingly used for minimally invasive *in vivo* imaging, in miniaturized microscopes and in lab-on-a-chip devices. Owing to optical aberrations and lower numerical apertures, a main class of microlens, gradient refractive index lenses, has not achieved resolution comparable to conventional microscopy. Here we describe high-resolution microlenses, and illustrate two-photon imaging of dendritic spines on hippocampal neurons and dual-color nonlinear optical imaging of neuromuscular junctions in live mice.

New applications enabled by small optical elements and their low costs are driving a rising usage of micro-optics in biomedicine. Applications in animals include minimally invasive imaging of cells in solid tissues, such as the brain and muscles, or in hollow organ tracts[1–4]. Miniaturized microscopes (~1 g mass) based on micro-optics[5,6] permit imaging in freely moving animals[6]. Diagnostics are also arising that involve cellular-level imaging in live subjects[7–9]. Emerging lab-on-a-chip devices rely on micro-optics in combination with microfluidics[10]. Collectively, there are multiple realms in which micro-optics will become increasingly crucial.

A main class of microlenses used for fluorescence imaging is gradient refractive index (GRIN) lenses, which generally have numerical aperture (NA) values $\leq$ 0.6. These elements provide superior image quality compared to other microlenses and have enabled the first commercial fluorescence microendoscopes for small-animal and clinical applications[7,9]. However, owing to their optical aberrations and lower NA values, GRIN lenses do not provide optical resolution comparable to that of conventional microscopy. The best Rayleigh resolution values achieved by two-photon fluorescence imaging with GRIN lenses are ~1.6 μm (lateral) and ~12 μm (axial), yielding highly elongated point spread functions that impede acquisition of high-quality, three-dimensional image stacks[4,5]. By comparison, a diffraction-limited 0.8 NA two-photon imaging system provides ~15 times greater voxel density with 920 nm laser excitation. The loss of resolution impairs image quality and hinders examination of micrometer-scale details. Increasing NA values and correcting aberrations are essential to improving the excitation and collection of signal photons while preserving images' fine features.

Here we report aberration-corrected imaging by combining GRIN lenses with high-NA plano-convex lenses cut from tiny, mass-produced ball lenses (**Fig. 1a**). Joining the two in series yielded micro-objectives with NA $\leq$ 0.85. A high-index glass, such as LaSFN9 (refractive index = 1.856), for the plano-convex element permitted high NA values and ~200% greater light collection compared to a single GRIN lens. However, plano-convex lenses introduce considerable spherical aberration, which must be compensated to attain high optical resolution. Thus, once we chose a plano-convex element, we made a matched GRIN lens with a refractive index profile tuned so that the primary spherical aberrations of the two elements cancel on the optical axis. We achieved this by calculating how fourth-order (n_{r4}) variations in the GRIN lens's radial refractive index profile, $n(r) = n_0 + n_{r2}\, r^2 + n_{r4}\, r^4 + \ldots$, affected spherical aberrations (**Supplementary Fig. 1**) and then tuning the GRIN fabrication silver-ion exchange process in glass rods[11] to yield index profiles optimally matched to our plano-convex lenses (Online Methods).

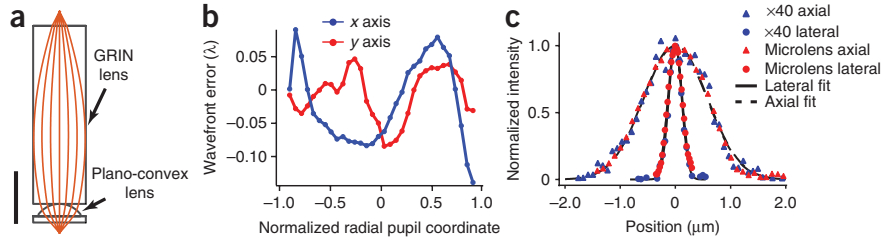

Figure 1 | Aberration-corrected micro-objectives enable high-resolution imaging. (**a**) Optical ray diagram of micro-objectives combining a plano-convex high-index lens and a 1.0-mm-diameter GRIN lens (0.45 NA) with an adapted index profile, yielding compound microlenses with NA $\leq$ 0.85. Scale bar, 1 mm. (**b**) Wavefront errors in units of λ measured by shearing interferometry[12] using light of 633 nm, as a function of normalized radial position (0 = on axis, 1.0 = the lens perimeter) across two orthogonal axes of the back pupil of a 0.82 NA micro-objective of 230 μm working distance in water. (**c**) Lateral and axial resolution measurements, using 920-nm excitation to image a 100-nm-diameter fluorescent bead, for a 0.82 NA micro-objective (microlens) and a water-immersion Olympus LUMPlan FI/IR 0.8 NA ×40 objective (×40). The bead's cross-sectional profiles in the lateral and axial dimensions are shown with Gaussian curve fits (fit), which are nearly indistinguishable from fits to the square of an Airy disc. Mean ± s.e.m. Rayleigh resolution values (1.0 ± 0.2 μm, lateral; 4.4 ± 0.2 μm, axial) were determined using n = 12 beads and measurements of this type.

[1]James H. Clark Center for Biomedical Engineering and Sciences, Stanford University, Stanford, California, USA. [2]GRINTECH GmbH, Jena, Germany. [3]Howard Hughes Medical Institute, Stanford University, Stanford, California, USA. Correspondence should be addressed to M.J.S. (mschnitz@stanford.edu).

RECEIVED 2 MARCH; ACCEPTED 12 MAY; PUBLISHED ONLINE 14 JUNE 2009; DOI:10.1038/NMETH.1339

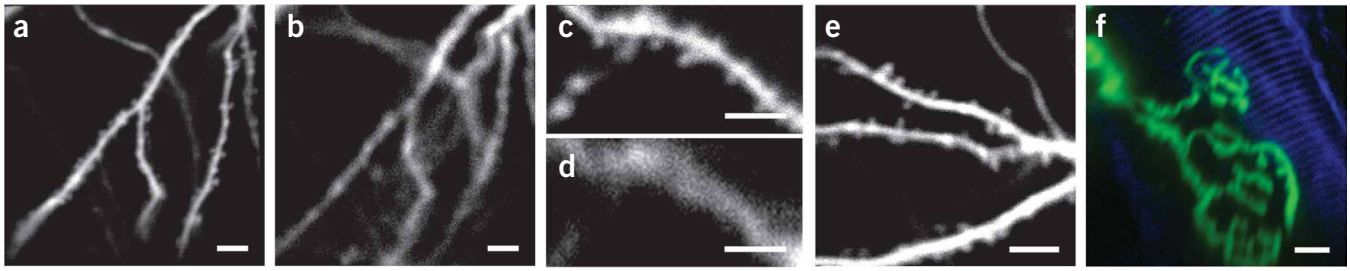

Figure 2 | *In vivo* two-photon imaging with high-resolution micro-objectives permits superior resolution than with uncorrected GRIN lenses and enables visualization of neuronal dendritic spines. (**a**–**e**) Images of GFP-expressing hippocampal pyramidal neurons in live mice. Images in **a**,**c**,**e** were acquired using a 0.82 NA micro-objective; **b** and **d** are corresponding images of the cells shown in **a** and **c**, acquired with a 0.48 NA singlet silver-doped GRIN objective. The image in **f** was obtained by dual-color imaging of a neuromuscular junction with the 0.82 NA micro-objective. Two-photon fluorescence from a YFP-expressing motor neuron (green) and second-harmonic generation from sarcomeres (blue) of the post-synaptic muscle. Images in **a**,**b**,**e**,**f** are 512 × 512 pixels. Images in **c**,**d** were cropped to 256 × 128 pixels. Scale bars, 5 μm (**a**–**e**) and 10 μm (**f**). All images but that in **e** are axial projections of three-dimensional image stacks (see Online Methods for parameters).

We validated our strategy for a 1-mm-diameter micro-objective of 230 μm working distance and 0.82 NA that we created for two-photon microscopy. By phase-shifting shearing interferometry[12] we measured the residual aberrations across 90% of the micro-objective's back aperture and found that the root mean square wavefront errors were only 5% of a wavelength, under conditions designed to approximate imaging in tissue (**Fig. 1b** and **Supplementary Fig. 2**). This degree of error is consistent with diffraction-limited performance[13]. After integrating our micro-objectives into a laser-scanning instrument for two-photon fluorescence imaging, the Rayleigh resolution values determined using 100-nm-diameter fluorescent beads and 920-nm excitation (1.0 ± 0.2 μm, lateral; 4.4 ± 0.2 μm, axial; mean ± s.e.m.; $n = 12$ beads) matched those of a water-immersion 0.80 NA microscope objective (Olympus ×40 LUMPlan FI/IR) (**Fig. 1c**). These values are consistent with diffraction-limited performance given the degree of laser beam expansion on our two-photon microscope (Prairie Technologies), which has a standard configuration.

To test image quality, we compared images of GFP-expressing CA1 hippocampal pyramidal neurons in live mice, as acquired with an aberration-corrected microlens or a conventional GRIN objective (**Fig. 2**). These comparisons revealed the improvement in lateral resolution attained by the corrected micro-objective as well as its superior optical sectioning ability, apparent via the reduced number of dendrites in individual images. Images obtained with the corrected microlens required reduced illumination power and often revealed neurons' dendritic spines (**Fig. 2a**,**c**,**e**). Spines were largely unresolved in images obtained with the conventional GRIN lens (**Fig. 2b**,**d**) and were not visible in previous neuronal imaging studies with GRIN microlenses[2,14]. Given that two-photon imaging of neocortical dendritic spines near the brain surface has propelled *in vivo* studies of neuronal structural plasticity[15], the resolution of dendritic spines with micro-optics might similarly enable plasticity studies in deep brain areas such as hippocampus. A second demonstration of microlens performance demanding resolution of fine details involved simultaneous second-harmonic and two-photon imaging of muscle fibers and neuromuscular junctions, yielding dual-color images (**Fig. 2f**).

In conclusion, economical and simply made micro-objectives can provide on-axis resolution comparable to that of commercial water-immersion objectives. A range of working distances and magnifications will be attainable by modest variations in the refractive index profile or by using different glasses for the plano-convex element. These microlenses should be an immediate enabling technology for a wide range of applications in research, pharmaceutical and biotechnology settings.

METHODS

Methods and any associated references are available in the online version of the paper at http://www.nature.com/naturemethods/.

Note: Supplementary information is available on the Nature Methods website.

ACKNOWLEDGMENTS

We thank the US National Institute of Neurological Disorders and Stroke (M.J.S.), GRINTech GmbH (B.M.) and the Stanford Biophysics (R.P.J.B.) training grant from the US National Institutes of Health for support of our work. We thank A. Attardo, L.D. Burns, E. Ho, J. Kobelke, S. Plochowietz and D. Profitt for technical assistance.

COMPETING INTERESTS STATEMENT

The authors declare competing financial interests: details accompany the full-text HTML version of the paper at http://www.nature.com/naturemethods/.

Published online at http://www.nature.com/naturemethods/
Reprints and permissions information is available online at http://npg.nature.com/reprintsandpermissions/

1. Flusberg, B.A. *et al. Nat. Methods* **2**, 941–950 (2005).
2. Levene, M.J., Dombeck, D.A., Kasischke, K.A., Molloy, R.P. & Webb, W.W. *J. Neurophysiol.* **91**, 1908–1912 (2004).
3. Alencar, H., Mahmood, U., Kawano, Y., Hirata, T. & Weissleder, R. *Neoplasia* **7**, 977–983 (2005).
4. Flusberg, B.A., Jung, J.C., Cocker, E.D., Anderson, E.P. & Schnitzer, M.J. *Opt. Lett.* **30**, 2272–2274 (2005).
5. Engelbrecht, C.J., Johnston, R.S., Seibel, E.J. & Helmchen, F. *Opt. Express* **16**, 5556–5564 (2008).
6. Flusberg, B.A. *et al. Nat. Methods* **5**, 935–938 (2008).
7. Hsiung, P.L. *et al. Nat. Med.* **14**, 454–458 (2008).
8. Llewellyn, M.E., Barretto, R.P., Delp, S.L. & Schnitzer, M.J. *Nature* **454**, 784–788 (2008).
9. Lin, K.Y., Maricevich, M., Bardeesy, N., Weissleder, R. & Mahmood, U. *Transl. Oncol.* **1**, 84–94 (2008).
10. Roulet, J.C. *et al. Anal. Chem.* **74**, 3400–3407 (2002).
11. Messerschmidt, B., McIntyre, B.L. & Houde-Walter, S.N. *Appl. Opt.* **35**, 5670–5676 (1996).
12. Sickenger, H., Falkenstoerfer, O.R., Lindlein, N. & Schwider, J. *Opt. Eng.* **33**, 2680–2686 (1994).
13. Born, M. & Wolf, E. *Principles of Optics* (Cambridge University Press, Cambridge, UK, 1999).
14. Jung, J.C., Mehta, A.D., Aksay, E., Stepnoski, R. & Schnitzer, M.J. *J. Neurophysiol.* **92**, 3121–3133 (2004).
15. Knott, G. & Holtmaat, A. *Brain Res. Rev.* **58**, 282–289 (2008).

ONLINE METHODS

Laser-scanning imaging. We used a commercial laser-scanning microscope (Prairie Technologies) equipped with a wavelength-tunable, ultrashort-pulsed Ti:sapphire laser (Mai-Tai; Spectra-Physics) and mechanically modified as described below to accommodate the addition of a micro-optical objective[8,14,16]. For all imaging sessions, the center wavelength of the laser pulses was set to 920 nm. For two-photon resolution measurements and imaging of GFP, we used a 525/50 ET emission filter (Chroma). For combined second-harmonic and YFP imaging, we split the emission into two channels using a 495 dichroic mirror (Semrock), and used 460/40 ET and 525/50 ET emission filters (Chroma).

For resolution measurements (**Fig. 1c**), and *in vivo* imaging of muscle (**Fig. 2f**) the microlens was held just beneath the microscope objective[8,14,16]. This involved the use of a two-pronged pincer holder (Micro-V-Clamp; Thorlabs) that gripped the microlens on its sides. This holder was attached to a miniature rotatable probe clamp (MXC-2.5; Siskiyou), which could be rotated about its long axis and swung in and out of the optical pathway. By adjusting the two angular degrees of freedom of the probe clamp, we aligned the microlens with the microscope objective, which coupled light in and out of the microlens[8,14,16]. Adjustments in the axial position of the microscope objective while keeping the microlens held fixed were accomplished using a stepper motor (MP-285; Sutter) mounted on the microscope's nosepiece. These adjustments modified the intermediate plane at which the illumination was focused above the microlens, leading to corresponding focal adjustments in the specimen. The microlens and microscope objective could also be moved in tandem using the microscope's normal focusing actuator. After positioning the specimen under the micro-objective, the intermediate focal plane was adjusted to be just above the top face of the microlens, and the microscope objective and microlens were lowered together until the specimen was in focus. For imaging of hippocampal neurons in live mice (**Fig. 2a–e**), the microlens was not held in its pincer clamp. Rather, the microlens was gently placed into a capillary guide tube that had been surgically implanted into the mouse's brain[6], as described below. Firmly securing the mouse within its head holder was sufficient to permit stable imaging. In this case, fine focal adjustment was only available by moving the microscope objective.

Micro-objectives. To construct a 0.82 NA micro-objective capable of near diffraction-limited performance, we combined a 1.0-mm-diameter plano-convex lens made of LaSFN9 glass (190-μm central thickness) with a 1.0-mm-diameter GRIN lens (0.45 NA). The length of the GRIN lens with the adapted index profile was 3.80 mm or 3.75-mm (0.35 pitch) for micro-objectives of 50-μm and 230-μm working distance, respectively. The GRIN lens was capped at the tip with a cover disk of 120-μm-thick BK7 glass. We protected and fixed the GRIN and plano-convex elements within a stainless steel sheath (1.0 mm inner diameter and 1.4 mm outer diameter) using optical epoxy. The data shown in **Figure 1c** are the resolution measurements for the 230-μm working distance lens, but corrected lenses of both 50-μm and 230-μm working distances produced comparable resolution measurements.

We designed GRIN lens refractive index profiles using ZEMAX software to minimize aberrations as in **Supplementary Figure 1**, and then fabricated the GRIN lenses by silver-ion exchange according to our published recipes, quantitative models of ion diffusion and tolerances[11,17,18]. Borosilicate glass rods with 25 mol% Na_2O content and a uniform refractive index of 1.51 were baked in a 20 mol% melt of $AgNO_3$ salts at $\sim 670^\circ$ K for approximately 3 weeks. This 'ion stuffing' step leads to a near total ($\sim 88\%$) and uniform exchange of the Na ions with Ag ions, raising the mass of the glass by 51% and the refractive index to 1.65. The rods were then returned to a melt of Na_2O at $\sim 750^\circ$ K for approximately 3 h for 'ion burying'. This re-exchanges Ag ions for Na ions, but to a much lesser extent as in the original exchange and preferentially on the rods' perimeters owing to the reduced time for exchange. The ion burying step leaves the refractive index just below 1.65 on the optical axis, but falling off smoothly with radius to a value just above 1.51 at the perimeter. For a given plano-convex element and corresponding desired GRIN profile, the duration of ion burying was adjusted slightly so as to yield different n_{r4} values. The glass rods were diced to the appropriate lengths using a diamond wheel blade and then polished. Corrected microlenses of this type will be commercially available from GRINTECH, GmbH.

Shearing interferometery. Phase-shifting shearing interferometry[12] was performed to assess wavefront aberrations under conditions designed to approximate those in tissue (**Supplementary Fig. 2**). For a micro-objective of 230 μm working distance in water, we mimicked the spherical aberration produced by light propagation across this distance of water by calculating the thickness of a BK7 cover glass needed to produce comparable aberrations. This calculation accounted for the difference in wavelengths used for two-photon imaging and by the shearing interferometer, and the resulting cover glass thickness was 320 μm. We made a BK7 cover glass of this thickness and attached it to the tip of the corrected micro-objective (**Supplementary Fig. 2**). We then placed the micro-objective into the shearing interferometer, which provided an assessment of wavefront aberrations by interferometrically comparing two copies of a coherent beam that passed through the micro-objective, with one copy laterally shifted relative to the other.

In this instrument a collimated 633 nm laser beam was focused by a coupling objective (Olympus ×40, 0.65 NA) to the image plane just outside the GRIN element of the compound microlens, corresponding to the top focal spot shown in **Figure 1a**. The resulting focal spot in the micro-objective's specimen plane was re-collimated by another objective (Olympus ×60, 0.80 NA) and then analyzed by the shearing interferometer to determine the wavefront errors arising within the micro-objective across 90% of its aperture. This first involved calibration of any wavefront errors induced by the microscope objectives alone, without the microlens inserted into the beam path. The wavefront errors of the micro-objective could then be determined by subtracting the errors induced by the objectives. A beamsplitter cube produced two copies of the laser beam, one of which could be laterally shifted relative to the other using mirror 1 (**Supplementary Fig. 2**). The two beams were reflected back into the beamsplitter cube, and the resulting fringe pattern of the recombined beams was recorded by a charge-coupled device (CCD) camera. Mirror 2 could be translated, permitting different amounts of phase shift to be introduced into one of the two beams. Multiple images of

the fringe patterns were recorded, each with different values of the phase shift, so as to allow more precise parametric fits to the wavefront errors across the beam profile. These fits were performed using the numerical methods described in ref. 12, yielding the data shown in **Figure 1b**.

Resolution measurements. Using two-photon fluorescence excitation and 920 nm laser illumination we imaged 100-nm-diameter fluorescent beads (Polysciences Inc.) that were fixed to a glass specimen slide and held under water immersion. Three-dimensional image stacks were acquired by displacing the specimen in 210-nm axial increments with a piezoelectric positioning system (Physik Instrumente). Optical magnifications were measured for each bead studied by moving the bead in all three dimensions through known distances.

To determine resolution values, lateral and axial intensity profiles of the bead images were fit to Gaussian curves, which are numerically indistinguishable from the square of an Airy disc to several significant figures. We determined the full-width-at-half-maximum (FWHM) of each curve fit and then converted this measure of resolution to the corresponding Rayleigh value by using a conversion factor of 1.65 for lateral and 1.57 for axial resolution measurements. We computed these factors by finding the ratio between the FWHM of the ideal two-photon point spread function and the Rayleigh resolution value, which is the distance from the central maximum of the point spread function to the first zero. Note that many prior publications describing resolution measurements, including those of our own laboratory, report FWHM values, not Rayleigh values. Our measurements revealed that the resolutions attained with the 50-μm and 230-μm working distance micro-objectives were comparable at their prescribed working distances.

Animal subjects, surgery and *in vivo* imaging procedures. All animal procedures were approved by the Stanford Institutional Animal Care and Use Committee. Adult transgenic mice expressing fluorescent protein driven by the *Thy1* promoter (GFP-M and YFP-16 lines) were used for neuronal and muscle experiments, respectively. In all live-animal experiments, we anesthetized mice with gaseous isoflurane (1.5–2.5%; mixed with 2 l min^{-1} oxygen). Body temperature was maintained at 37 °C, and depth of anesthesia was assessed by monitoring pinch withdrawal, eyelid reflex and respiration rate.

For muscle imaging[8], after the mouse had reached a high plane of anesthesia, we shaved the mouse's hindlimb and held the limb within a stable metal frame. A small incision was made through the skin overlying the medial gastrocnemius muscle. Once the site of imaging was surgically exposed, we inserted the micro-objective into the muscle by moving the microlens and microscope objective in tandem as described above. The slight pressure from the micro-objective helped stabilize the tissue under view. We irrigated exposed tissue regularly with mammalian Ringer's solution.

For hippocampal imaging[6], we implanted glass capillary imaging guide tubes into the brain through a 2.0-mm-diameter craniotomy centered at 2.0–2.5 mm posterior to bregma and 2.0–2.5 mm lateral to bregma. These guide tubes were cut, polished and sealed at one end with a cover slip to allow optical but not physical access to tissue. Low-melting-point agarose was used to seal the craniotomy and stabilize the guide tube over the hippocampus. A sealing of dental acrylic was applied over exposed areas of the skull. A metal bar was affixed to the dental acrylic for future attachment to an imaging frame. After recovery from surgery, mice returned to their home cage for 1–2 weeks before imaging.

At the imaging session, the anesthetized mice were mounted to a frame via the metal head-bar that had been fixed surgically on the cranium. The implanted guide tube was aligned parallel to the optical axis, by adjusting the position of the mouse's head so that the back surface of the microlens appeared circular through the microscope eyepieces. The interior of the guide tube was cleaned to remove debris. The micro-objective was inserted to rest on the guide tube's optical window. Thus, unlike for muscle imaging, the micro-objective was mechanically coupled to the mouse, not the microscope. The microscope objective was then located over the micro-objective and lowered until the specimen was in focus.

Image parameters and processing. For two-photon imaging of hippocampal pyramidal neurons, with either an aberration-corrected micro-objective or a singlet GRIN objective, we used 920-nm illumination. Image stacks were acquired with an axial spacing between frames chosen to be approximately threefold smaller than the extent of the axial point spread function. Thus, with the corrected micro-objective, images were acquired at <1.5 μm spacing, but at <4 μm spacing with the 0.48 NA GRIN singlet lens. For *in vivo* imaging (**Fig. 2a–d,f**), eight consecutive three-dimensional stacks were acquired using brief dwell times (0.8 μs) for each pixel, owing to concerns about motion artifacts arising from the mouse's physiological rhythms. The individual images in a stack were registered to one another in the lateral dimensions to remove any rigid image displacements between the frames. The eight stacks were then averaged together and an average *z*-dimension projection was performed. Alternatively, in a mouse that exhibited very little motion from physiological rhythms, longer dwell times (4 μs) were usable (**Fig. 2e**), and frame averaging within individual imaging planes could be performed.

Lower excitation power was needed with the corrected micro-objective than with the GRIN singlet, owing to the former's larger collection NA and improved ability to excite two-photon fluorescence. Thus, illumination power at the specimen was 12, 25, 12, 25 and 4 mW for the data in **Figure 2a–e**. Data shown in **Figure 2a,c** are average *z*-dimension projections of four images acquired over a 4.2 μm axial range at 1.4 μm spacing. Data in **Figure 2b,d** are average *z*-dimension projections of three images acquired over a 5.0 μm axial range at 2.5 μm spacing. Data in **Figure 2e** is an average of 30 frames acquired at the same focal plane. For the image in **Figure 2f**, a stack of 79 frames was acquired at 1.16 μm axial spacing by gradually raising the power from 20 to 30 mW as the depth into tissue increased. All images were acquired at 12-bit resolution, thresholded to 8 bits and displayed using linear lookup tables.

16. Jung, J.C. & Schnitzer, M.J. *Opt. Lett.* **28**, 902–904 (2003).
17. Messerschmidt, B., Possner, U. & Houde-Walter, S.N. *Appl. Opt.* **36**, 8145–8152 (1997).
18. Messerschmidt, B., Possner, T. & Goering, R. *Appl. Opt.* **34**, 7825–7830 (1995).

doi:10.1038/nmeth.1339